REVIEW

Visualizing and discovering cellular structures with super-resolution microscopy

Yaron M. Sigal, Ruobo Zhou, Xiaowei Zhuang*

Super-resolution microscopy has overcome a long-held resolution barrier—the diffraction limit—in light microscopy and enabled visualization of previously invisible molecular details in biological systems. Since their conception, super-resolution imaging methods have continually evolved and can now be used to image cellular structures in three dimensions, multiple colors, and living systems with nanometer-scale resolution. These methods have been applied to answer questions involving the organization, interaction, stoichiometry, and dynamics of individual molecular building blocks and their integration into functional machineries in cells and tissues. In this Review, we provide an overview of super-resolution methods, their state-of-the-art capabilities, and their constantly expanding applications to biology, with a focus on the latter. We will also describe the current technical challenges and future advances anticipated in super-resolution imaging.

Fluorescence microscopy has been central in shaping our understanding of the molecular organization and interactions of biological systems. Its high molecular specificity and multicolor imaging capability allow direct visualization of interactions between specific molecular species, and its low invasiveness allows the study of living systems under physiological conditions. However, a main challenge in fluorescence microscopy was the limited spatial resolution set by the diffraction of light. This resolution limit, first described by Ernst Abbe in 1873, restricts the smallest objects that can be resolved by conventional light microscopes. As a result, objects separated by a distance smaller than approximately half of the wavelength of visible light, i.e., ~200 to 300 nm, are indistinguishable, making many molecular structures in cells unresolvable. The advent of super-resolution imaging methods has shattered this limit. In this Review, we will provide an overview of the methods that surpass the diffraction limit in the far field, with emphasis on the new biological insights afforded by these methods.

Overview of super-resolution imaging methods

The key to overcoming the diffraction limit lies in the ability to distinguish molecules that reside within the same diffraction-limited volume. This has been achieved by two main categories of approaches. The first category accomplishes this in a spatially coordinated manner by using patterned illumination to differentially modulate the fluorescence emission of molecules within the diffraction-limited volume and thereby achieve separate detection of these molecules. The pioneering method in this category is stimulated emission depletion (STED) microscopy (*1*, *2*), subsequently generalized to reversible saturable optical linear fluorescence transitions (RESOLFT) (*3*). STED and RESOLFT overcome the diffraction limit by accompanying a focused excitation beam with a spatially patterned "depletion" beam, typically in a donut shape, which serves to counteract excitation through either stimulated emission (STED) (*1*, *2*) or other types of fluorescence transitions, such as photoswitching (RESOLFT) (*3*). As a result, only molecules at the very center of the donut-shaped beam (where the laser intensity is near zero) can emit light, thus creating a region of fluorescence emission that is much smaller than a typical focal spot of the light microscope. The reverse strategy is also possible, with the donut beam serving as patterned activation rather than depletion, limiting the emission-free region instead of emission region to the center of the beam (*4*). Scanning these beams across the sample then generates an image with a resolution much higher than the diffraction limit. Various other illumination patterns can also be used to increase the spatial frequency of the emission region and hence the image resolution (*4*). For example, in structured illumination microscopy (SIM), the sample is excited by a series of standing waves with different orientations or phases to increase the spatial frequency detectable by the microscope (*5*). Because the standing-wave pattern is itself limited by diffraction, the linear form of SIM only extends the diffraction limit by a factor of 2, whereas the nonlinear form of SIM (NL-SIM) overcomes the diffraction limit by using the nonlinear or saturated response of fluorophores to further increase the spatial frequency of the emission pattern (*5*), similar to STED and RESOLFT (*4*). Unlike STED and RESOLFT, which generate super-resolution images directly from the recorded raw data, SIM and NL-SIM require additional computational treatment to reconstruct final images (*4*, *5*).

Howard Hughes Medical Institute, Department of Chemistry and Chemical Biology, Department of Physics, Harvard University, Cambridge, MA 02138, USA.
*Corresponding author. Email: zhuang@chemistry.harvard.edu

The second category of methods achieves the separation of molecules by stochastically turning on individual molecules within the diffraction-limited volume at different time points, including stochastic optical reconstruction microscopy (STORM) (*6*) and (fluorescence) photoactivated localization microscopy [(F)PALM] (*7*, *8*), and subsequent variations of these approaches (*9*, *10*). When isolated in space, the positions of individual molecules can be determined to nanometer or even subnanometer precision by localizing the center positions of their images (*11*–*13*). However, molecules within the same diffraction-limited volume generate overlapping images, which is the fundamental cause of the diffraction limit in resolution. STORM and PALM overcome this limit by switching on only a stochastic subset of fluorescent molecules within a field of view at any given time such that their images do not substantially overlap, allowing their positions to be localized with high precision; these molecules are then switched off (or bleached) and a stochastically different subset of molecules are switched on and localized—iterating this process allows a super-resolution image to be constructed from numerous molecular localizations accumulated over time (*6*–*8*). Such stochastic activation of molecules is typically achieved by using photoswitchable dyes or fluorescent proteins (*6*–*10*). A variety of photoswitchable probes have been used for this approach, in some cases leading to the creation of different acronyms subsequently, but the imaging principle is the same as that for STORM and PALM. In addition to using photoswitchable probes, transient binding of fluorescent probes can also be used to stochastically "turn on" fluorescent signals in space and time, as in point accumulation for imaging in nanoscale topography (PAINT) (*14*).

Recently, a new super-resolution imaging method named MINFLUX has been developed that combines strengths from both categories of approaches, by using stochastic switching of individual molecules to enable the separate detection of nearby molecules, along with patterned illumination, such as a donut-shaped beam, to achieve ultrahigh-precision localization of individual molecules by detecting local emission minima (*15*).

In addition to the above methods, which directly overcome the diffraction limit optically, a different form of super-resolution microscopy, expansion microscopy (ExM), has been recently developed, which increases the image resolution effectively through physical expansion of samples (*16*). In ExM, the specimen is embedded in a gel with the labeling probes attached to the gel. The sample is then digested to leave only the labeling probes attached to the gel followed by gel expansion to increase the probe separation, allowing super-resolution images to be taken with diffraction-limited microscopes.

Super-resolution technologies are constantly expanding, including both variations of the above approaches and other distinct methods, such as fluctuation-based methods and computer-vision–based methods. Owing to the limited space of this short review and its focus on biological applications, we cannot describe all methods here but

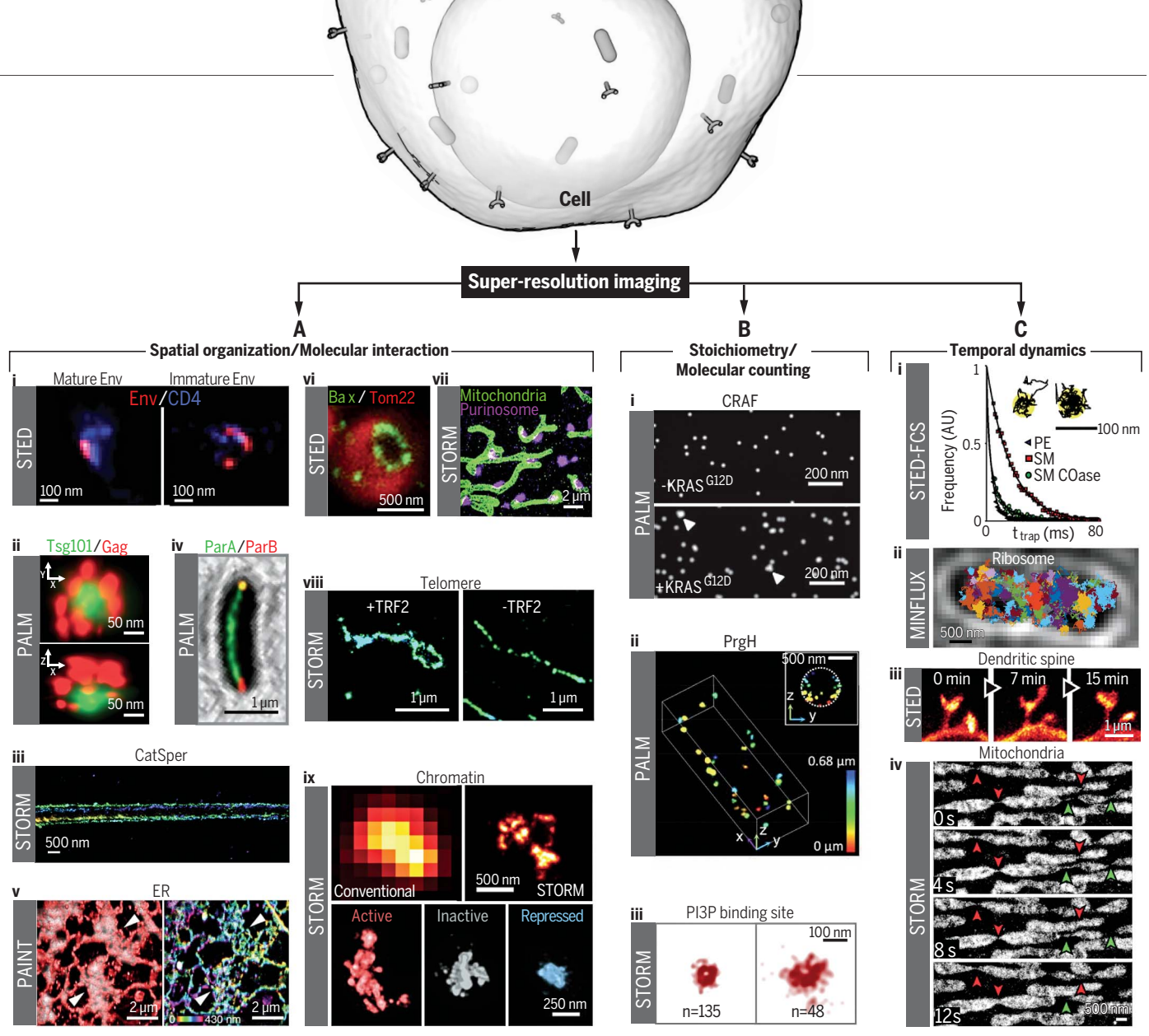

Fig. 1. Quantitative biological insights from three directions of applications of super-resolution imaging. (**A**) (**i**) STED images showing distinct distribution patterns of the envelope protein Env (red) in mature (left) and immature (right) HIV-1 particles attached to the cell, overlaid with the cell surface HIV-1 receptor CD4 (blue). (**ii**) PALM images showing the organization of ESCRT-I subunit Tsg101 (green) in an HIV assembly site marked by HIV Gag proteins (red) in lateral (top) and axial (bottom) views. (**iii**) 3D STORM images of a sperm-specific calcium channel (CatSper1) showing four linear domains along the sperm flagella. The *z*-position information is color-coded. (**iv**) PALM image on a bacterial cell showing the distribution of the ParA ATPase (green) with the ParB DNA binding protein (red) localized to the cell poles, for the coordination of chromosome segregation and cell division. (**v**) Left: Overlay of PAINT (red) and diffraction-limited (gray) images of the ER obtained using lattice light-sheet microscopy. Right: PAINT image from the left panel, but color-coded by the *z*-position information. White arrowheads indicate areas that appear as sheets in diffraction-limited images but are resolved as connected tubular structures in super-resolution images. (**vi**) STED image of the proapoptotic cell-death mediator Bax (green) showing ring structures in apoptotic mitochondria marked by Tom22 (red). (**vii**) STORM image showing interactions between mitochondria (green) and purinosomes marked by the core protein FGAMS (magenta). (**viii**) Comparison of STORM images of telomeric DNA in mouse embryo fibroblasts in the presence (left) and absence (right) of the shelterin protein TRF2 that is required for t-loop formation. (**ix**) Top: Comparison of diffraction-limited (left) and 3D STORM (right) images for DNA in a chromatin domain in the nucleus of *Drosophila* Kc167 cells. Bottom: Differential DNA compaction of transcriptionally active (red), inactive (gray), or polycomb-repressed (blue) epigenetic domains visualized using STORM. (**B**) (**i**) PALM images of proto-oncogene cRAF clusters on the cell plasma membrane, with (bottom) and without (top) coexpression of $KRAS^{G12D}$, which induces cRAF clustering. (**ii**) 3D PALM image of molecular clusters with various sizes formed by a secretion system protein PrgH near the membrane of a bacterial cell. (**iii**) STORM images of endocytic vesicles displaying distinct vesicle size and phosphatidylinositol 3-phosphate (PI3P) content. The number of PI3P binding sites on each vesicle (*n*) is indicated. (**C**) (**i**) Durations (t_{trap}) for three lipid types—phosphoethanolamine (PE, gray), sphingomyelin (SM, red), and sphingomyelin after cholesterol depletion (SM COase, green)—that are differentially trapped in ~20-nm nanodomains at the plasma membrane, which are detected and distinguished by STED-FCS and confocal single-molecule tracking. (**ii**) Single-particle tracking of a 30*S* ribosomal subunit protein in a bacterial cell by using MINFLUX. Trajectories of individual molecules are shown in different colors. (**iii**) Time-lapse STED images of a region of the somatosensory cortex of a living mouse with enhanced yellow fluorescent protein (EYFP)–labeled neurons, showing dynamics of dendritic spines. (**iv**) Time-lapse STORM images showing fission (green arrowheads) and fusion (red arrowheads) events of mitochondria, with thin tubular structures connecting neighboring mitochondria as fission and fusion intermediates. Figures are modified from the following sources: (A) i (*49*); ii (*50*); iii (*51*), with permission from Elsevier; iv (*52*), with permission from Springer Nature; v (*35*); vi (*54*); vii (*56*); viii (*59*), with permission from Elsevier; ix (*60*), with permission from Springer Nature; (B) i (*66*); ii (*67*); iii (*64*); (C) i (*69*); ii (*15*); iii (*71*); iv (*34*).

refer interested readers to other reviews (*4*, *9*, *10*) for additional coverage on super-resolution technologies.

Imaging capabilities of super-resolution microscopy

Three-dimensional (3D) imaging

The 3D nature of biological structures calls for super-resolution in all three dimensions. For methods based on stochastic activation of single molecules, such as STORM and PALM, achieving 3D super-resolution imaging requires high-precision localization not only in the *xy* plane, but also in the *z* direction along the optical axis. This was first achieved by astigmatism imaging [by using a cylindrical lens to create *z*-dependent point-spread-function (PSF)] (*17*), followed by various other approaches including bifocal plane imaging (*18*), PSF engineering (*19*), and interferometry (*20*), among others (*9*, *10*, *21*). In STED and RESOLFT, isotropic 3D super-resolution imaging was achieved by generating a depletion illumination pattern to counteract excitation in all directions surrounding the focal point—for example, by using a donut-shaped STED beam in conjunction with two opposing objectives (*4*, *22*).

Image resolution

Both the methods based on patterned illumination, like STED, RESOLFT, and NL-SIM, and the methods based on single-molecule switching and localization, like PALM and STORM, are diffraction-unlimited, and thus do not have a theoretical resolution limit. In practice, however, many factors can influence the achievable resolution, including the excitation and detection schemes, and the photophysical properties and size of fluorescent probes, as well as the labeling and sampling density of these probes. In biological applications, resolutions achieved by these methods are typically in the range of 10 to 70 nm, with sub–10 nm resolution achieved in some cases (*9*, *10*).

For the patterned-illumination–based methods, the spatial frequency (or sharpness) of the final emission pattern determines the image resolution. For example, in STED and RESOLFT, the donut-shaped depletion beam limits the fluorescence emission zone to the very center of the donut beam. The stronger the depletion light, the narrower this emission zone and the higher the achievable image resolution (*4*). However, strong illumination can lead to substantial photobleaching, phototoxicity, and enhanced background noise. Hence, the resolutions typically achieved are tens of nanometers, although resolution as high as a few nanometers has also been demonstrated by using probes with ultrahigh photostability, such as diamond nitrogen-vacancy centers (*4*). With isoSTED, isotropic 3D resolution of ~30 nm has been demonstrated (*4*, *22*). Combining patterned illumination with photoswitchable probes, RESOLFT (*3*, *4*) has also achieved ~30-nm isotropic 3D resolution (*23*). Similarly, by combining sinusoidal patterned illumination and photoswitchable probes, and using additional computational image reconstruction, NL-SIM has demonstrated ~45- to 60-nm resolution in 2D using saturated depletion (SD NL-SIM) or patterned activation (PA NL-SIM) (*24*, *25*). PA NL-SIM has been extended to 3D with the help of lattice light sheet microscopy (*26*), providing a resolution of ~120 to 230 nm in 3D (*25*).

For single-molecule-switching–based methods, such as STORM and PALM, the resolution depends on the photophysical properties of the fluorophores. Although many fluorophores exhibit blinking or switching behavior, only those with sufficient brightness and proper on-off switching kinetics yield high-quality images (*27*). The achievable image resolution depends on the number of photons detected from individual molecules, known as the photon budget. Typical experiments with bright photoswitchable dyes provide ~20- to 30-nm *xy* resolution, whereas the resolution is worse for fluorescent proteins because of their lower photon budget. The resolution is often worse in the *z* direction, but the use of interferometry (*20*, *28*, *29*) or specially engineered PSF (*30*) can improve the *z* resolution to become equal to or even better than the *xy* resolution. For example, interferometry can provide <10-nm *z* resolution, though a more complicated imaging setup is needed (*20*, *28*, *29*). In general, the resolution in both *xy* and *z* directions can be increased by improving the photon budget of the fluorophores. For example, the development of ultrabright photoactivatable dyes allowed a resolution as high as a few nanometers to be achieved on biological structures using STORM (*31*). More recently, using stochastic binding of dye-labeled DNA probes, DNA-PAINT also achieved similar image resolution on DNA-origami nanostructures (*32*). However, the time required to detect such a large number of photons for each molecule substantially increased the acquisition time per image. The recently developed MINFLUX thus represents an important advance in that it uses patterned excitation to drastically increase the localization precision (or reduce the number of photons required to reach a set precision), achieving an impressive localization precision of ~1 nm with an orders-of-magnitude lower photon budget (*15*). In ExM, the resolution depends on the number of rounds of sample expansion and the expansion factor per round, and a resolution of ~25 nm has been demonstrated with two rounds of expansion (*33*).

Other factors can also limit the final image resolution, such as the size of the fluorescent probes and the labeling density, which affect all super-resolution methods. For single-molecule–based approaches, methods that increase the number of times each target is sampled can also increase the final resolution if the resolution is limited by sampling density. This includes using fluorophores that undergo many on-off switching cycles (*27*), diffusible probes that can sample multiple locations of the target (*34*), and PAINT approaches that sample the target numerous times using reversible probe binding (*35*).

Finally, thick samples pose additional challenges, including reduced localization precision for out-of-focus molecules, optical aberration, and light scattering, as well as increase in background noise, all of which can lower image resolution. Various PSF engineering methods have been developed to allow high localization precision over substantially longer focal depths (*19*, *21*, *30*). Adaptive optics have been used to correct for aberrations in super-resolution imaging of thick samples (*29*), and light-sheet illumination provides an effective optical-sectioning approach to reduce background in thick-sample super-resolution imaging (*36*). Tissue clearing methods can reduce not only aberration but also scattering and are particularly powerful for thick-sample imaging (*37*). Alternatively, serial physical sectioning has also been used to reconstruct super-resolution images over large volumes of tissue (*38*).

Live-cell imaging, temporal resolution, and phototoxicity

Several super-resolution methods have demonstrated live-cell imaging. As scanning-based techniques, STED and RESOLFT can image a relatively small field of view (FOV) with very high temporal resolution, and thus have the impressive capability of probing millisecond dynamics of cellular structures at the spatial resolution of tens of nanometers (*39*). Although the time resolution decreases with increasing FOVs, highly parallelized RESOLFT with 100,000 intensity minima, effectively akin to 100,000 tightly spaced donut patterns, allows subsecond time resolution for large FOVs (*40*).

As widefield imaging methods, the time resolutions of STORM and PALM do not change as rapidly with the FOV size. Subsecond time resolution at ~20- to 30-nm spatial resolution has been achieved for large FOVs in live-cell imaging by STORM using fast-switching dyes (*41*) and fast scientific-CMOS cameras (*42*). Several recently developed algorithms to localize a high density of molecules with overlapping images (*43*) can further increase the time resolution of these methods. In addition, the single-particle–tracking mode of PALM, STORM, and PAINT (*44*, *45*) allows movement of individual molecules to be tracked with time resolutions of milliseconds to tens of milliseconds at high molecular concentrations. The ability of MINFLUX to achieve high localization precision with a minimal photon budget has led to a drastic increase in the tracking time resolution of molecules in live cells to the submillisecond scale (~100 μs), coupled with a corresponding increase in the number of snapshots possible for each molecule before photobleaching (*15*).

For live-cell imaging, in addition to achieving high spatiotemporal resolution, it is also important to reduce photobleaching and phototoxicity to prolong the overall duration of imaging and to minimize perturbations to the biological systems. Because of the trade-offs between spatial and temporal resolutions and between spatiotemporal resolution and phototoxicity/imaging duration, it is possible to reduce the spatial resolution of both the patterned-illumination-based methods, such as STED and RESOLFT, and the single-molecule-switching–based methods, such as STORM and PALM, to trade for higher time resolution, or lower phototoxicity and longer imaging duration.

In addition, adaptively changing the intensity of the STED beam based on the presence or absence of fluorophores, as in DyMIN, results in a substantial reduction in photobleaching and phototoxicity (*46*). By using photoswitching instead of stimulated emission, RESOLFT requires a much lower light intensity than STED, and thus drastically reduces phototoxicity in live-cell super-resolution imaging (*4*). When the spatial resolution requirement is not particularly high (~100 nm), SIM is a popularly used live-cell imaging method because of its capability for high-speed widefield imaging with low phototoxicity. The recently reported PA NL-SIM demonstrated live-cell imaging with ~60-nm spatial resolution and subsecond time resolution over large FOVs and tens of time points (*25*). In general, using light-sheet illumination for optical sectioning can also reduce phototoxicity in imaging (*36*). The recently developed lattice light sheet microscopy (*26*) further decreases phototoxicity and improves optical sectioning (to ~300 nm) compared to previous light-sheet schemes, and has been used in conjunction with super-resolution approaches to improve their volumetric live-cell imaging capability (*25*, *26*, *35*).

Quantitative biological insights offered by super-resolution imaging

Super-resolution imaging has transformed our understanding of biological systems and the applications are rapidly expanding, prohibiting comprehensive descriptions in a short review. Instead, we will highlight in this section the types of quantitative insights that can be obtained by super-resolution imaging, with representative examples illustrating each case (Fig. 1). In the next section, we will provide more detailed descriptions of a few examples to further illustrate the power of super-resolution imaging (Figs. 2 to 4).

Spatial organization and molecular interaction of cellular structures

The nanometer-scale resolution afforded by super-resolution imaging has substantially advanced our

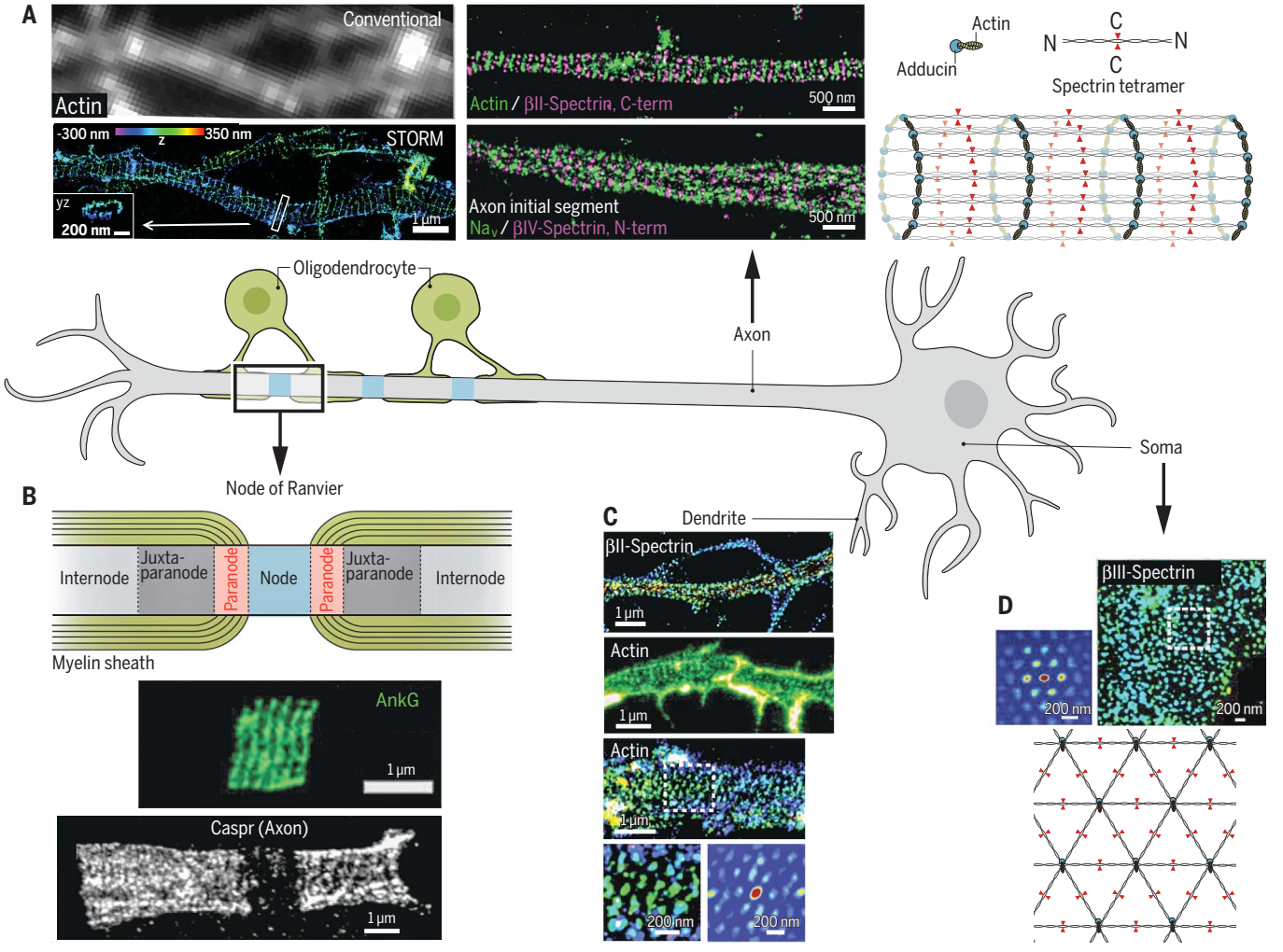

Fig. 2. The membrane-associated periodic skeleton (MPS) in neurons discovered by super-resolution imaging. (**A**) Quasi-1D periodic MPS observed in axons by using STORM. Left: Comparison of diffraction-limited (top) and 3D-STORM (bottom) images of actin in axons. STORM image shows the periodic distribution of actin rings along the axon that is obscured by diffraction-limited imaging. Middle: Two-color STORM images showing the periodic distributions of and spatial relationship between actin, spectrins (βII- and βIV-spectrin), and voltage-gated sodium channels (Na_v). Right: Schematic of the 1D MPS structure showing the organization of actin, spectrin tetramers, and adducin. Modified from (*47*). (**B**) Top: Schematic of a node of Ranvier. Center: STED image showing the periodic distribution ankyrin-G (AnkG) on the 1D MPS structure at a node of Ranvier. Modified from (*74*). Bottom: STED image showing the periodic distribution of the adhesion molecule Caspr on the 1D MPS structure observed flanking a node of Ranvier. Modified from (*76*). (**C**) MPS structures observed in dendrites: Top: 1D MPS in a dendritic region observed by STORM imaging of βII-spectrin. Modified from (*72*). Upper middle: 1D MPS observed in a dendritic region by STED imaging of actin. Modified from (*73*). Lower middle: 2D polygonal lattice-like arrangement of MPS components observed in a dendritic region by STORM imaging of actin. Bottom: A magnified region of the STORM image (left) and the corresponding 2D autocorrelation analysis (right) are shown. Modified from (*77*). (**D**) 2D MPS observed on the soma of neuron by STORM imaging of βIII-spectrin (top right) along with a 2D autocorrelation analysis of the boxed region (top left). Bottom: Schematic of the 2D MPS structure. Modified from (*77*).

ability to interrogate the spatial organization of molecular structures in cells (*9*, *10*). In addition, multicolor super-resolution imaging has allowed molecular interactions to be examined at unprecedented resolution (*9*, *10*). With these abilities, super-resolution imaging has provided new insights into numerous cellular structures, and even led to discoveries of previously unknown cellular structures, such as the membrane-associated periodic skeleton (MPS) in neurons (*47*) detailed in the next section.

At the cell surface, membrane proteins such as receptors, channels, vesicle scission proteins, and viral fusion proteins have been investigated by various super-resolution approaches and are often found to assume functionally important spatial organizations. For example, it was shown that the SNARE complex component syntaxin-1 is densely packed within discrete clusters that are regulated by the lipid composition (*48*). The HIV envelope protein (Env) was observed to reorganize upon maturation, which is important for viral entry (*49*) (Fig. 1A, i), whereas the ESCRT complex is localized to the virus budding site and plays an important role in HIV budding (*50*) (Fig. 1A, ii). The calcium channel CatSper was shown to adopt a linear-domain organization along the sperm tail together with other signaling and scaffolding molecules, playing an important role in calcium signaling and sperm activity (*51*) (Fig. 1A, iii). In the cytoplasm, super-resolution imaging has provided new insights into the organization of cytoskeleton structures and membrane organelles, as well as other molecular assemblies. In addition to the discovery of the MPS in neurons (*47*), as will be detailed in the next section, novel organization has also been observed for other cytoskeletal structures, such as the ParA/ParB system in bacteria (*52*) (Fig. 1A, iv) and focal adhesions connecting the cytoskeleton to the plasma membrane (*53*). For membrane organelles, super-resolution imaging has revealed, for example, densely packed and dynamic tubular structures in endoplasmic reticulum (ER) sheets (*35*) (Fig. 1A, v), ring structures of Bax on apoptotic mitochondria (*54*, *55*) (Fig. 1A, vi), and synergistic interactions between mitochondria and purinosomes (*56*) (Fig. 1A, vii). In addition to protein structures, super-resolution imaging has also provided new insights into RNA distributions and interactions in cells (*57*, *58*). In the cell nucleus, super-resolution imaging has revealed interesting organizations of DNA and DNA-interacting proteins, such as the TRF2-dependent telomere loop (t-loop) formation important for DNA end protection (*59*) (Fig. 1A, viii), distinct chromatin organization and compaction in different epigenetic states (*60*) (Fig. 1A, ix), and cell-type–dependent organizations of nucleosomes (*61*).

Stoichiometry of molecular complexes

Although measuring stoichiometry by spatially resolving individual subunits within molecular complexes is still challenging, the ability to activate and localize individual molecules by PALM and STORM has triggered growing interest in stoichiometric characterizations within intact cells. However, it is important to note that the number of measured single-molecule localizations is not equivalent to the number of molecules because of two complications. The first arises from imperfect labeling. New labeling approaches, such as using gene editing to label endogenous proteins with rapidly maturing, monomeric fluorescent proteins or with protein or peptide tags that can be conjugated to dyes with near 100% efficiency, can help mitigate this challenge. The second complication arises from complex fluorophore switching: No dye or fluorescent protein has the ability to give precisely one localization per molecule because fluorophores blink (multiple times), and most fluorophores also have an inactivatable fraction. Multiple methods have been developed to combat this problem, including calibrations of fluorophores using standards of known stoichiometry or quantification and modeling of blinking properties (*62*–*64*). STED has also been used to quantify the number of molecules based on coincident photon detection (*65*). These methods have been applied to quantifying, for example, the number of proteins in flagellar motors (*62*), receptor complexes (*63*), kinase complexes (*66*) (Fig. 1B, i), and secretion machinery (*67*) (Fig. 1B, ii), as well as the number of lipid binding sites in endocytic vesicles (*64*) (Fig. 1B, iii).

Temporal dynamics of cellular structures

Super-resolution imaging has enhanced our ability to extract dynamic information of cellular structures, allowing the mobility of biomolecules and the shape or structural dynamics of molecular complexes and organelles to be tracked with higher accuracy. For example, STED imaging has been used in combination with fluorescence correlation spectroscopy (FCS) to study the diffusion properties of molecules on the membrane. The drastic reduction in the region of fluorescence emission by the STED beam has allowed the detection of membrane nanodomains <20 nm in size, within which different lipid molecules show distinct diffusion properties (*68*, *69*) (Fig. 1C, i). Super-resolution imaging has also enhanced our ability to perform single-particle tracking (SPT) in live cells. Conventional SPT experiments require a low labeling density for the molecule of interest to avoid signal overlap between molecules. Stochastically turning on only a subset of labeled molecules at a given time, as in PALM, STORM, and PAINT, allows SPT at much higher molecular concentrations at the endogenous expression level (*34*, *44*, *45*), facilitating the studies of gene expression, protein–nucleic acid interaction, and dynamic processes on cell membranes. With its unique capabilities, MINFLUX has allowed the tracking of ribosomes in bacterial cells with unprecedented spatiotemporal resolution, achieving a localization precision of <50 nm with a time resolution of ~100 μs (*15*) (Fig. 1C, ii).

In addition, various super-resolution microscopy methods have been used to measure structural and shape dynamics of molecular assemblies, organelles and small cellular compartments, such as the dynamics of neuronal processes and dendritic spines in tissue (*70*) and even in live animals (Fig. 1C, iii) (*71*), fission and fusion dynamics of mitochondria (*34*) (Fig. 1C, iv), and structural dynamics of ER (*35*).

Super-resolution studies of specific molecular assemblies

The membrane-associated periodic skeleton in neurons

Super-resolution imaging enabled the discovery of the membrane-associated periodic skeleton (MPS) in neurons, which was initially observed in the axons by STORM imaging (*47*). In the MPS, short actin filaments, capped by actin-capping proteins, such as adducin, are organized into repetitive, ring-like structures that wrap around the circumference of the axon; adjacent actin rings are connected by spectrin tetramers, forming a long-range quasi-1D periodic structure with a periodicity of ~180 to 190 nm underneath the axonal membrane (*47*) (Fig. 2A).

The MPS spans the entire axon shaft, in both myelinated and unmyelinated axonal segments, including the axon initial segments (AIS) and nodes of Ranvier where action potentials are generated and amplified, respectively (*47*, *72*–*76*) (Fig. 2, A and B). This structure was observed in all neuronal types examined, including excitatory and inhibitory neurons in both central and peripheral nervous systems (*74*, *75*), and is evolutionarily conserved across diverse animal species (*75*). Subsequent to its discovery in axons, this 1D periodic structure was also observed in dendrites by both STORM and STED (*72*, *73*) (Fig. 2C), but the formation propensity and development rate of MPS appear to be lower in dendrites than in axons (*77*). In addition, a 2D polygonal lattice structure formed by MPS components was observed in the soma and dendrites (Fig. 2D), resembling the membrane skeleton structure observed in erythrocytes (*77*).

This highly ordered submembrane skeletal structure can play diverse functional roles in neurons. It provides flexible mechanical support for axons that is likely critical for axon stability under mechanical stress (*47*); indeed, axons tend to break in spectrin-deficient animals under movement-induced stress (*78*). The MPS was also implicated in mechanosensation (*79*). Moreover, the MPS organizes membrane proteins, such as ion channels and adhesion molecules, into periodic distributions along axons (*47*, *72*, *73*, *76*), potentially influencing the generation and propagation of action potentials, and other signaling pathways in axons. The MPS also influences axon and dendrite morphology (*80*), is important for the formation of the AIS and nodes of Ranvier (*72*, *76*, *80*), and may also act as a diffusion barrier at the AIS (*81*). Disruption of the MPS causes widespread neurodegeneration and a range of neurological impairments (*80*), and mutations of MPS components are implicated in various neurodegenerative diseases. The discovery of the MPS, which escaped detection by previous imaging methods, demonstrates the power of

super-resolution imaging for uncovering new cellular structures.

Molecular organization in synapses

Neuronal synapses are typically only several hundred nanometers in size but contain elaborate protein machineries to orchestrate neurotransmitter-mediated signal transmission; hence, the structural interrogation of synapses requires high spatial resolution and has benefited from extensive super-resolution imaging efforts. For example, STED has revealed the spatial organization of several important components within the *Drosophila* neuromuscular junction, including the clustered organization of Ca^{2+} channels, as well as the organization of scaffolding proteins required for both Ca^{2+} channel clustering and synaptic vesicle tethering at the presynaptic active zone (*82*, *83*) (Fig. 3A). STORM imaging has mapped the spatial organization of many proteins in the pre- and postsynaptic terminals, which show oriented organization of presynaptic scaffolding proteins, laminar organization of postsynaptic density proteins, and synapse-to-synapse variability in the lateral distributions of neurotransmitter receptors (*84*) (Fig. 3B).

In addition, recent super-resolution studies revealed that the neurotransmitter receptors and postsynaptic scaffolding proteins adopt activity-dependent clustered organization (*85*, *86*) (Fig. 3C). Such clustered organization also extends across the synaptic cleft, giving rise to "nanocolumns" formed by spatially aligned presynaptic vesicle fusion sites and postsynaptic receptor clusters (*87*) (Fig. 3D). This nanocolumn organization provides a mechanism for the coordination of synaptic vesicle release and neurotransmitter receptor response.

Super-resolution studies of synapses have been recently extended to both proteomic-scale analysis of synaptic structures and circuit-scale analysis of synapse distributions. For example, STED has been used to image numerous protein components in the presynaptic terminals, creating a model of an "average" synaptic bouton (*88*). A

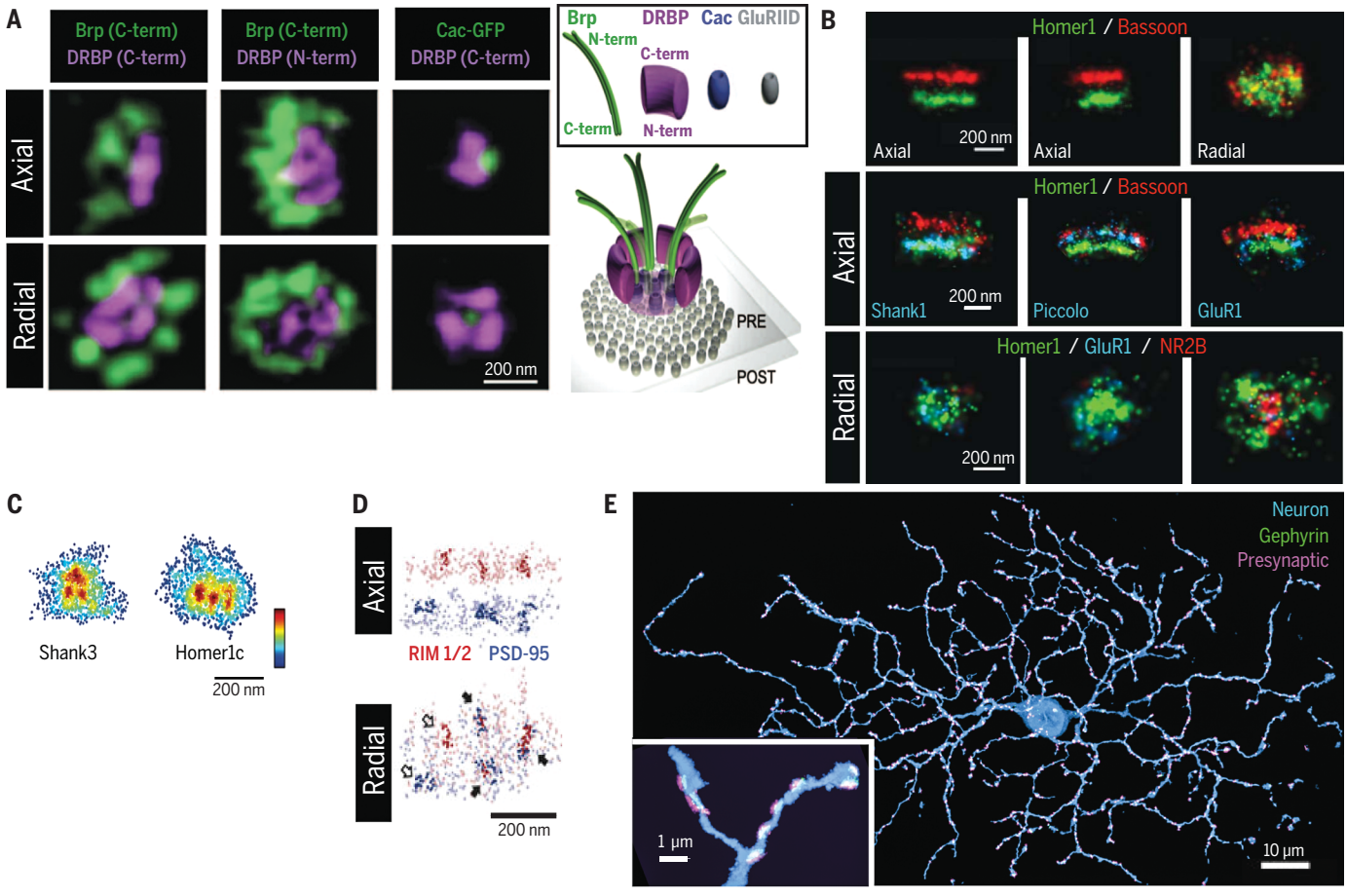

Fig. 3. Super-resolution imaging of synaptic structures. (**A**) Left: 3D STED images of the presynaptic active zone including Bruchpilot (Brp) and *Drosophila* RIM binding protein (DRBP), as well as the voltage-gated calcium channel Cacophony (Cac) at *Drosophila* neuromuscular junction synapses. Both axial (top) and radial (bottom) projections are shown. Right: Schematic of the active zone showing positions and orientations of components of the active zone cytomatrix including Brp, DRBP, and Cac in relation to the postsynaptic glutamate receptor (GluRIID) determined by using STED. Modified from (*83*). (**B**) Top: 3D STORM images of presynaptic protein Bassoon (red) and postsynaptic protein Homer (green). Two orthogonal axial views (left and middle) and the radial view (right) are shown. Center: Axial views of three synapses. In addition to Bassoon (red) and Homer1 (green), a third color (blue) was used to map the positions of additional postsynaptic (Shank1, left; GluR1, right) and presynaptic (Piccolo, middle) components at synapses. Bottom: Radial views of three example synapses showing differential abundance and spatial distribution of neurotransmitter receptors, NR2B and GluR1. Modified from (*84*) with permission from Elsevier. (**C**) Radial projections of PALM images showing the clustered organization of postsynaptic proteins Shank3 (left) and Homer1c (right). Modified from (*85*) with permission from Elsevier. (**D**) STORM and PALM images show that areas of higher protein density (darker colors) of both presynaptic (RIM1/2, red) and postsynaptic (PSD-95, blue) components are often trans-synaptically aligned to form "nanocolumns" (indicated by filled arrows). Both axial (top) and radial (bottom) projections are shown. Modified from (*87*) with permission from Springer Nature. (**E**) STORM maximum intensity projection of a retinal ganglion cell (blue) with associated synapses marked by postsynaptic scaffolding protein gephyrin (green) and presynaptic proteins (Bassoon, Piccolo, Munc13-1, and ELKS) (magenta), reconstructed from ultrathin serial sections. Inset shows a magnified view of a region of dendrite. Modified from (*38*) with permission from Elsevier.

volumetric STORM platform has been developed to determine the entire synaptic fields of neurons (*38*) (Fig. 3E), providing synaptic connectivity at the neural circuit scale.

Protein complexes with structural symmetry

On the shorter length scale of individual protein complexes, it is possible to obtain higher-resolution reconstructions from many super-resolution images through particle averaging in a way that is similar to electron microscopy (EM) reconstruction, especially for structures with well-defined symmetry. Two notable examples are centrioles and nuclear pore complexes (NPCs).

STED and STORM, the latter in combination with particle averaging, have been used to visualize the ninefold symmetry of centrioles (*89*, *90*) (Fig. 4A). In addition to resolving this symmetric arrangement, super-resolution imaging has also been used to map the 3D organization of several centriolar proteins and determine the order of protein recruitment during centriole formation (*91*, *92*). At centrosomes, centrioles are surrounded by the less structured pericentriolar material (PCM), and the radial distribution of proteins within the centrosome and PCM have also been mapped by STORM and SIM (*93*, *94*) (Fig. 4, B and C).

Similarly, STORM imaging showed the eightfold radial symmetry of NPCs (*95*) (Fig. 4D). In combination with particle averaging, STORM allowed the positions of seven nucleoporin components to be determined with ~1-nm precision, which in turn allowed the orientation of the Nup107-160 subcomplex within the pore to be determined (*96*). These super-resolution pictures allowed discrimination between contradictory models of the structural organization of the NPC scaffold (*96*) (Fig. 4E).

Outlook

Super-resolution fluorescence microscopy has transformed understanding of the structure and function of many biological systems. However, challenges are still present, and to maximize the impact of super-resolution microscopy, further technological advancements are still needed.

The spatial resolution achieved by super-resolution microscopy in biological systems typically ranges from 10 to 70 nm, larger than most biomolecules. Achieving true molecular-scale resolution (~1 nm) would allow molecular interactions and conformations to be directly probed inside cells, but remains a challenging task. In principle, the two main categories of optical approaches to overcome the diffraction limit, including the patterned-illumination–based methods represented by STED, RESOLFT, and NL-SIM and the single-molecule-switching–based methods represented by STORM, PALM, and PAINT, can both achieve unlimited high resolution. However, practical factors, such as the requirement of increasing illumination intensity (in the former category) and increasing fluorophore photon budget (in the latter category) for higher resolution, limit the resolution that can be achieved. Reinspection of the fundamental principles of super-resolution methods can lead to powerful new innovations and concepts, as demonstrated by MINFLUX, which combines strengths from both approaches and achieves ultrahigh, previously inaccessible, resolutions. In addition, these methods can be combined with ExM, an orthogonal approach that achieves resolution increase through physical sample expansion, potentially leading to a direct multiplication in the fold increases in resolution that are separately achievable by individual methods. However, it is worth noting that the final image resolution is also limited by probe size and labeling density. Thus, to ultimately benefit from the ultrahigh resolution, parallel development in probes and labeling methods is needed to allow molecules in cells to be labeled with small-molecule probes with high efficiency.

Furthermore, although super-resolution imaging has demonstrated subsecond and even millisecond time resolution in some cases, owing to the trade-off between spatial and temporal resolutions, the limited photon budget of the fluorophores, and phototoxicity to samples, live-cell imaging with high spatiotemporal resolution for a long period of time remains difficult and an active area of development. In addition, in vivo super-resolution imaging deep inside tissues remains challenging, notwithstanding considerable efforts combating tissue-induced background, aberration, and light scattering.

Another challenge, but also an exciting new direction, is to increase the number of molecular species that can be simultaneously imaged. Cells contain thousands of distinct genes and other molecules that act collectively to give rise to behavior and function, yet multicolor imaging usually only allows simultaneous visualization of a few different molecular species. Recent advances have broken new ground in this direction, and genomic-scale imaging is now within reach. For example, single-cell transcriptome-imaging methods have allowed RNAs of 1000 or more genes to be simultaneously imaged in individual cells by using multiplexed fluorescence in situ hybridization (FISH) (*97*, *98*) or in situ sequencing (*99*, *100*). A similar level of multiplexity

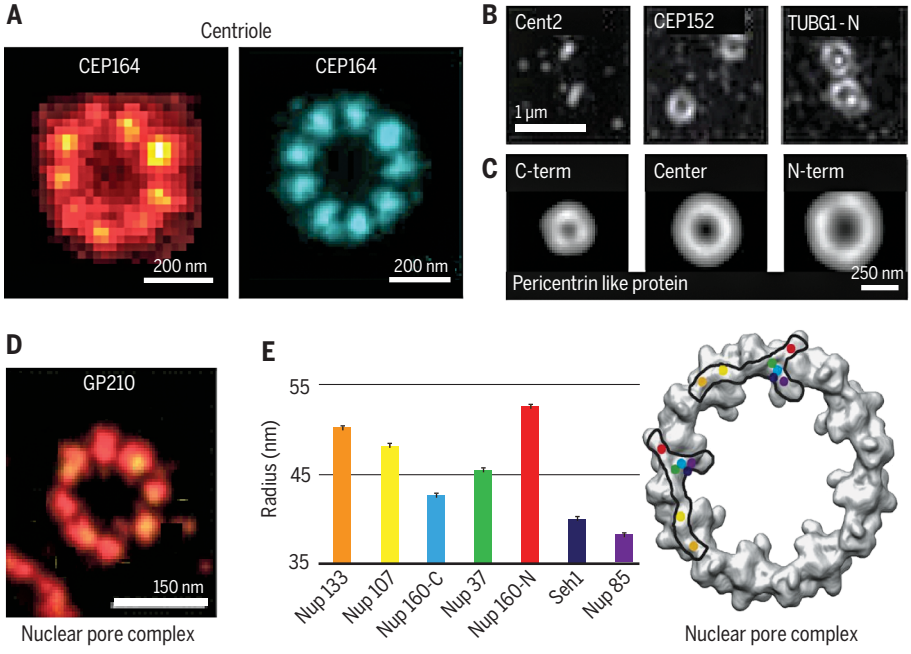

Fig. 4. Super-resolution visualizing molecular complexes: Centriole-containing complexes and the nuclear pore complex. (**A**) Single STED image (left) and particle-averaged STORM image (right) of the centriolar protein (CEP164), showing a radial ninefold symmetry. STED image modified from (*89*) with permission from Elsevier; STORM image modified from (*90*) with permission from Springer Nature. (**B**) Three centriolar and pericentriolar proteins—Cent2, CEP152 and γ-tubulin (TUBG1), imaged using SIM showing a concentric organization of the pericentriolar matrix. Modified from (*93*) with permission from Springer Nature. (**C**) Average distribution of C-terminus, central domain, and N-terminus of the pericentrin-like protein (PLP) demonstrating a radial, spoke-like orientation for PLP through the pericentriolar matrix as determined by SIM. Modified from (*94*) with permission from Springer Nature. (**D**) Single STORM image of the nucleoporin protein GP210 showing an eightfold symmetry within the nuclear pore complex of *Xenopus* oocytes. Modified from (*95*). (**E**) Left: Radial distribution of several nucleoporins including Nup133, Nup107, Nup160 (C-terminus), Nup37, Nup160 (N-terminus), Seh1, and Nup85, that comprise the Y-shaped Nup107-160 complex determined using STORM and particle averaging. Right: A projection of the electron density of the cytoplasmic ring of the NPC determined by EM is overlaid with two possible arrangements of the Nup107-160 complex, determined by super-resolution imaging. Each protein is represented by a colored dot corresponding to the color and radius in the graph (left). Modified from (*96*).

may be achievable for DNA and proteins in the future. Combination of these approaches with super-resolution microscopy could potentially allow genomic-scale super-resolution imaging. Technologically, a major challenge in genomic-scale imaging is molecular crowding, which can prevent resolution of neighboring molecules by conventional imaging, and super-resolution microscopy provides a promising solution. Biologically, the ability to image all molecules in a complex molecular machinery or in a whole signaling pathway, and ultimately at the whole-genome scale, will provide a comprehensive picture of the molecular basis of cellular behavior and function. It is exhilarating to imagine how such a picture of a cell, with all molecules imaged at a resolution that allows direct inference of molecular interactions, would open new opportunities for understanding life at the molecular level.

REFERENCES AND NOTES

1. S. W. Hell, J. Wichmann, *Opt. Lett.* **19**, 780–782 (1994).
2. T. A. Klar, S. W. Hell, *Opt. Lett.* **24**, 954–956 (1999).
3. M. Hofmann, C. Eggeling, S. Jakobs, S. W. Hell, *Proc. Natl. Acad. Sci. U.S.A.* **102**, 17565–17569 (2005).
4. C. Eggeling, K. I. Willig, S. J. Sahl, S. W. Hell, *Q. Rev. Biophys.* **48**, 178–243 (2015).
5. R. Heintzmann, M. G. L. Gustafsson, *Nat. Photonics* **3**, 362–364 (2009).
6. M. J. Rust, M. Bates, X. Zhuang, *Nat. Methods* **3**, 793–796 (2006).
7. E. Betzig *et al*., *Science* **313**, 1642–1645 (2006).
8. S. T. Hess, T. P. Girirajan, M. D. Mason, *Biophys. J.* **91**, 4258–4272 (2006).
9. B. Huang, H. Babcock, X. Zhuang, *Cell* **143**, 1047–1058 (2010).
10. S. J. Sahl, S. W. Hell, S. Jakobs, *Nat. Rev. Mol. Cell Biol.* **18**, 685–701 (2017).
11. W. E. Moerner, M. Orrit, *Science* **283**, 1670–1676 (1999).
12. A. Yildiz *et al*., *Science* **300**, 2061–2065 (2003).
13. A. Pertsinidis, Y. Zhang, S. Chu, *Nature* **466**, 647–651 (2010).
14. A. Sharonov, R. M. Hochstrasser, *Proc. Natl. Acad. Sci. U.S.A.* **103**, 18911–18916 (2006).
15. F. Balzarotti *et al*., *Science* **355**, 606–612 (2017).
16. F. Chen, P. W. Tillberg, E. S. Boyden, *Science* **347**, 543–548 (2015).
17. B. Huang, W. Wang, M. Bates, X. Zhuang, *Science* **319**, 810–813 (2008).
18. M. F. Juette *et al*., *Nat. Methods* **5**, 527–529 (2008).
19. S. R. Pavani *et al*., *Proc. Natl. Acad. Sci. U.S.A.* **106**, 2995–2999 (2009).
20. G. Shtengel *et al*., *Proc. Natl. Acad. Sci. U.S.A.* **106**, 3125–3130 (2009).
21. A. von Diezmann, Y. Shechtman, W. E. Moerner, *Chem. Rev.* **117**, 7244–7275 (2017).
22. R. Schmidt *et al*., *Nat. Methods* **5**, 539–544 (2008).
23. U. Böhm, S. W. Hell, R. Schmidt, *Nat. Commun.* **7**, 10504 (2016).
24. E. H. Rego *et al*., *Proc. Natl. Acad. Sci. U.S.A.* **109**, E135–E143 (2012).
25. D. Li *et al*., *Science* **349**, aab3500 (2015).
26. B. C. Chen *et al*., *Science* **346**, 1257998 (2014).
27. G. T. Dempsey, J. C. Vaughan, K. H. Chen, M. Bates, X. Zhuang, *Nat. Methods* **8**, 1027–1036 (2011).
28. D. Aquino *et al*., *Nat. Methods* **8**, 353–359 (2011).
29. F. Huang *et al*., *Cell* **166**, 1028–1040 (2016).
30. S. Jia, J. C. Vaughan, X. Zhuang, *Nat. Photonics* **8**, 302–306 (2014).
31. J. C. Vaughan, S. Jia, X. Zhuang, *Nat. Methods* **9**, 1181–1184 (2012).
32. M. Dai, R. Jungmann, P. Yin, *Nat. Nanotechnol.* **11**, 798–807 (2016).
33. J. B. Chang *et al*., *Nat. Methods* **14**, 593–599 (2017).
34. S. H. Shim *et al*., *Proc. Natl. Acad. Sci. U.S.A.* **109**, 13978–13983 (2012).
35. J. Nixon-Abell *et al*., *Science* **354**, aaf3928 (2016).
36. A. K. Gustavsson, P. N. Petrov, W. E. Moerner, *Opt. Express* **26**, 13122–13147 (2018).
37. V. Gradinaru, J. Treweek, K. Overton, K. Deisseroth, *Annu. Rev. Biophys.* **47**, 355–376 (2018).
38. Y. M. Sigal, C. M. Speer, H. P. Babcock, X. Zhuang, *Cell* **163**, 493–505 (2015).
39. J. Schneider *et al*., *Nat. Methods* **12**, 827–830 (2015).
40. A. Chmyrov *et al*., *Nat. Methods* **10**, 737–740 (2013).
41. S. A. Jones, S. H. Shim, J. He, X. Zhuang, *Nat. Methods* **8**, 499–505 (2011).
42. F. Huang *et al*., *Nat. Methods* **10**, 653–658 (2013).
43. D. Sage *et al*., *Nat. Methods* **12**, 717–724 (2015).
44. S. Manley *et al*., *Nat. Methods* **5**, 155–157 (2008).
45. G. Giannone *et al*., *Biophys. J.* **99**, 1303–1310 (2010).
46. J. Heine *et al*., *Proc. Natl. Acad. Sci. U.S.A.* **114**, 9797–9802 (2017).
47. K. Xu, G. Zhong, X. Zhuang, *Science* **339**, 452–456 (2013).
48. G. van den Bogaart *et al*., *Nature* **479**, 552–555 (2011).
49. J. Chojnacki *et al*., *Science* **338**, 524–528 (2012).
50. S. B. Van Engelenburg *et al*., *Science* **343**, 653–656 (2014).
51. J.-J. Chung *et al*., *Cell* **157**, 808–822 (2014).
52. J. L. Ptacin *et al*., *Nat. Cell Biol.* **12**, 791–798 (2010).
53. P. Kanchanawong *et al*., *Nature* **468**, 580–584 (2010).
54. L. Große *et al*., *EMBO J.* **35**, 402–413 (2016).
55. R. Salvador-Gallego *et al*., *EMBO J.* **35**, 389–401 (2016).
56. J. B. French *et al*., *Science* **351**, 733–737 (2016).
57. J. Fei *et al*., *Science* **347**, 1371–1374 (2015).
58. J. R. Moffitt, S. Pandey, A. N. Boettiger, S. Wang, X. Zhuang, *eLife* **5**, e13065 (2016).
59. Y. Doksani, J. Y. Wu, T. de Lange, X. Zhuang, *Cell* **155**, 345–356 (2013).
60. A. N. Boettiger *et al*., *Nature* **529**, 418–422 (2016).
61. M. A. Ricci, C. Manzo, M. F. García-Parajo, M. Lakadamyali, M. P. Cosma, *Cell* **160**, 1145–1158 (2015).
62. S.-H. Lee, J. Y. Shin, A. Lee, C. Bustamante, *Proc. Natl. Acad. Sci. U.S.A.* **109**, 17436–17441 (2012).
63. M. Renz, B. R. Daniels, G. Vámosi, I. M. Arias, J. Lippincott-Schwartz, *Proc. Natl. Acad. Sci. U.S.A.* **109**, E2989–E2997 (2012).
64. E. M. Puchner, J. M. Walter, R. Kasper, B. Huang, W. A. Lim, *Proc. Natl. Acad. Sci. U.S.A.* **110**, 16015–16020 (2013).
65. H. Ta *et al*., *Nat. Commun.* **6**, 7977 (2015).
66. X. Nan *et al*., *Proc. Natl. Acad. Sci. U.S.A.* **110**, 18519–18524 (2013).
67. Y. Zhang, M. Lara-Tejero, J. Bewersdorf, J. E. Galán, *Proc. Natl. Acad. Sci. U.S.A.* **114**, 6098–6103 (2017).
68. C. Eggeling *et al*., *Nature* **457**, 1159–1162 (2009).
69. S. J. Sahl, M. Leutenegger, M. Hilbert, S. W. Hell, C. Eggeling, *Proc. Natl. Acad. Sci. U.S.A.* **107**, 6829–6834 (2010).
70. J. Tønnesen, V. V. G. K. Inavalli, U. V. Nägerl, *Cell* **172**, 1108–1121.e15 (2018).
71. S. Berning, K. I. Willig, H. Steffens, P. Dibaj, S. W. Hell, *Science* **335**, 551 (2012).
72. G. Zhong *et al*., *eLife* **3**, e04581 (2014).
73. E. D'Este, D. Kamin, F. Göttfert, A. El-Hady, S. W. Hell, *Cell Reports* **10**, 1246–1251 (2015).
74. E. D'Este *et al*., *Sci. Rep.* **6**, 22741 (2016).
75. J. He *et al*., *Proc. Natl. Acad. Sci. U.S.A.* **113**, 6029–6034 (2016).
76. E. D'Este, D. Kamin, F. Balzarotti, S. W. Hell, *Proc. Natl. Acad. Sci. U.S.A.* **114**, E191–E199 (2017).
77. B. Han, R. Zhou, C. Xia, X. Zhuang, *Proc. Natl. Acad. Sci. U.S.A.* **114**, E6678–E6685 (2017).
78. M. Hammarlund, E. M. Jorgensen, M. J. Bastiani, *J. Cell Biol.* **176**, 269–275 (2007).
79. M. Krieg, A. R. Dunn, M. B. Goodman, *Nat. Cell Biol.* **16**, 224–233 (2014).
80. C. Y. Huang, C. Zhang, D. R. Zollinger, C. Leterrier, M. N. Rasband, *J. Neurosci.* **37**, 11323–11334 (2017).
81. D. Albrecht *et al*., *J. Cell Biol.* **215**, 37–46 (2016).
82. R. J. Kittel *et al*., *Science* **312**, 1051–1054 (2006).
83. K. S. Y. Liu *et al*., *Science* **334**, 1565–1569 (2011).
84. A. Dani, B. Huang, J. Bergan, C. Dulac, X. Zhuang, *Neuron* **68**, 843–856 (2010).
85. H. D. MacGillavry, Y. Song, S. Raghavachari, T. A. Blanpied, *Neuron* **78**, 615–622 (2013).
86. D. Nair *et al*., *J. Neurosci.* **33**, 13204–13224 (2013).
87. A. H. Tang *et al*., *Nature* **536**, 210–214 (2016).
88. B. G. Wilhelm *et al*., *Science* **344**, 1023–1028 (2014).
89. L. Lau, Y. L. Lee, S. J. Sahl, T. Stearns, W. E. Moerner, *Biophys. J.* **102**, 2926–2935 (2012).
90. X. Shi *et al*., *Nat. Cell Biol.* **19**, 1178–1188 (2017).
91. L. Gartenmann *et al*., *Curr. Biol.* **27**, R1054–R1055 (2017).
92. V. Hamel *et al*., *Curr. Biol.* **27**, 2486–2498.e6 (2017).
93. S. Lawo, M. Hasegan, G. D. Gupta, L. Pelletier, *Nat. Cell Biol.* **14**, 1148–1158 (2012).
94. V. Mennella *et al*., *Nat. Cell Biol.* **14**, 1159–1168 (2012).
95. A. Löschberger *et al*., *J. Cell Sci.* **125**, 570–575 (2012).
96. A. Szymborska *et al*., *Science* **341**, 655–658 (2013).
97. K. H. Chen, A. N. Boettiger, J. R. Moffitt, S. Wang, X. Zhuang, *Science* **348**, aaa6090 (2015).
98. S. Shah *et al*., *Cell* **174**, 363–376.e16 (2018).
99. X. Wang *et al*., *Science* **361**, eaat5691 (2018).
100. J. H. Lee *et al*., *Science* **343**, 1360–1363 (2014).

ACKNOWLEDGMENTS

Funding: This work is in part supported by the National Institutes of Health. X.Z. is a Howard Hughes Medical Institute Investigator.
Competing interests: None declared.

10.1126/science.aau1044

Visualizing and discovering cellular structures with super-resolution microscopy

Yaron M. Sigal, Ruobo Zhou and Xiaowei Zhuang

Science **361** (6405), 880-887.
DOI: 10.1126/science.aau1044